

Tetramode Metamaterials as Phonon Polarizers

Michael Fidelis Groß, Jonathan Ludwig Günter Schneider, Yu Wei, Yi Chen, Sebastian Kalt, Muamer Kadic, Xiaoning Liu, Genkai Hu,* and Martin Wegener*

In classical Cauchy elasticity, 3D materials exhibit six eigenmodes of deformation. Following the 1995 work of Milton and Cherkaev, extremal elastic materials can be classified by the number of eigenmodes, N , out of these six that are “easy”. Using Greek number words, this leads to hexamode ($N = 6$), pentamode ($N = 5$), tetramode ($N = 4$), trimode ($N = 3$), dimode ($N = 2$), and monomode ($N = 1$) materials. While hexamode materials are unstable in all regards, the possibility of pentamode metamaterials (“meta-fluids”) has attracted considerable attention throughout the last decade. Here, inspired by the 2021 theoretical work of Wei, Liu, and Hu, microstructured 3D polymer-based tetramode metamaterials are designed and characterized by numerical band-structure calculations, fabricated by laser printing, characterized by ultrasound experiments, and compared to the theoretical ideal. An application in terms of a compact and broadband polarizer for acoustical phonons at ultrasound frequencies is demonstrated.

generalization of the 1D Hooke’s spring constant to 3D materials leads to the classical Cauchy elasticity tensor.^[1,2] In three dimensions, this elasticity tensor can be represented by a 6×6 matrix (in Voigt notation).^[1,2] Therefore, Cauchy elastic materials generally exhibit six orthogonal eigenmodes of deformation. For special extremal cases, some of the corresponding eigenvalues may be very small compared to the others or even zero. This means that these eigenmodes are “easy” in the sense that no force or energy is required to induce the corresponding deformation.^[3] The number of easy eigenmodes, $N = 1, 2, 3, 4, 5$, and 6 , can be used to name extremal materials in Cauchy elasticity.^[3–6] Using Greek number words, this leads to hexamode ($N = 6$), pentamode ($N = 5$), tetramode ($N = 4$), tri-

mode ($N = 3$), dimode ($N = 2$), and monomode ($N = 1$) materials. While hexamode materials correspond to the absence of an elastic material and are hence trivial, the other five classes of extremal elastic materials potentially provide us with unusual and interesting mechanical properties.

About a decade ago, following a theoretical suggestion by Milton and Cherkaev,^[3] man-made architectures called pentamode metamaterials were introduced experimentally.^[7] Ideally, five of their elastic eigenmodes have strictly zero eigenvalues. In practice, the eigenvalue of one eigenmode is orders of magnitude larger than that of the other five eigenmodes. This behavior was achieved by approximating ideal hinges within a diamond-like lattice by thin connections between double-cone elements.^[7,8] In this manner, the compression of all double-cone elements is uneasy, whereas all other material deformations are easy. This equivalently means that the wave speed of longitudinally polarized phonons is much (ideally infinitely) larger than the wave speed of all transverse acoustical phonons, leading to a broad frequency interval in which only longitudinal phonons can propagate.^[8–10] Propagating transverse acoustical phonons are forbidden in this interval. Such behavior can be used for cloaking^[11–14] or as a longitudinal polarizer.^[9] As usual,^[15] transverse (longitudinal) phonons mean that the phonon displacement-vector \vec{u} is polarized perpendicular (parallel) to the phonon wavevector \vec{k} .

Such pentamode longitudinal elastic polarizer is distinct from a linear polarizer in optics, for which one transverse polarization is transmitted, whereas the orthogonal transverse polarization is suppressed.^[16–18] Longitudinal waves are usually absent in optics. Polarizers in optics can be realized by exploiting birefringent materials.^[19] For example, a birefringent

1. Introduction


According to Hooke’s law,^[1] linear elastic materials react with a deformation, the amplitude of which is proportional to the amplitude of the force field exerted onto them. The

M. F. Groß, Y. Chen, M. Kadic, M. Wegener
Institute of Nanotechnology
Karlsruhe Institute of Technology (KIT)
76128, Karlsruhe, Germany
E-mail: martin.wegener@kit.edu

M. F. Groß, J. L. G. Schneider, Y. Chen, S. Kalt, M. Wegener
Institute of Applied Physics
Karlsruhe Institute of Technology (KIT)
76128, Karlsruhe, Germany

Y. Wei, X. Liu, G. Hu
School of Aerospace Engineering
Beijing Institute of Technology (BIT)
Beijing 100081, P. R. China
E-mail: hugeng@bit.edu.cn

M. Kadic
Institut FEMTO-ST
UMR 6174
CNRS
Université de Bourgogne Franche-Comté (UBFC)
Besançon 25030, France

 The ORCID identification number(s) for the author(s) of this article can be found under <https://doi.org/10.1002/adma.202211801>.

© 2023 The Authors. Advanced Materials published by Wiley-VCH GmbH. This is an open access article under the terms of the Creative Commons Attribution License, which permits use, distribution and reproduction in any medium, provided the original work is properly cited.

DOI: 10.1002/adma.202211801

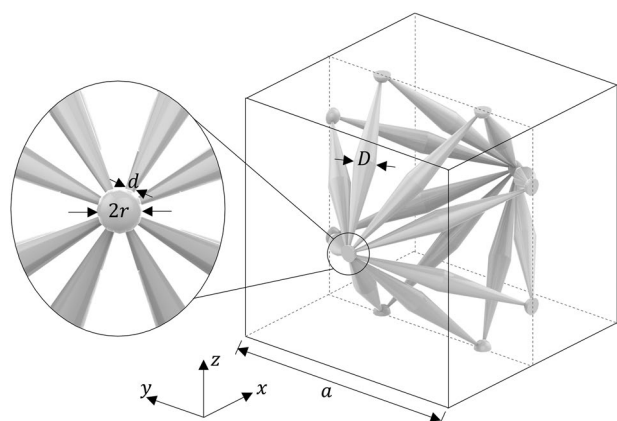


Figure 1. 3D model of the tetramode sample unit cell. The unit cell exhibits tetragonal symmetry and is placed onto a simple-cubic translation lattice with lattice constant a . The unit cell is constructed from double-cone elements connected by spheres of radius r . The crucial design parameters D and d are the diameter of the double-cone center and the diameter of the connection between double-cones and spheres, respectively. The spheres are chosen as connection hubs for the double-cone elements to obtain a well-defined geometry and to facilitate sample fabrication and the subsequent characterization using optical-image digital cross-correlation analysis and laser Doppler vibrometry. For the constituting material, we choose the parameters of Young's modulus $E = 4.19$ GPa, Poisson's ratio $\nu = 0.4$, and mass density $\rho = 1190$ kg m $^{-3}$ for the numerical calculations.

metamaterial can be constructed by a grid of parallel conducting metal wires with sub-wavelength spacing. Such grid polarizers are used in many commercial Fourier-transform spectrometers from the visible to the far infrared of the electromagnetic spectrum.^[18] According to the classification of Milton and Cherkaev,^[3] such an array of conductive metal wires (cf. Figure 1 in Reference^[18]) corresponds to a bimode metamaterial in electrical conduction (they spoke of a “bimode” metamaterial). Electrical conduction in three dimensions is conceptually much simpler than elasticity^[2] because one has only three orthogonal eigenmodes (rather than six in Cauchy elasticity).

Here, building on previous theoretical work on tetramode metamaterials (called “quadramode” metamaterials there),^[20,21] we present theory and experiments on tetramode elastic metamaterials. These unusual microstructured man-made materials are realized by tailored 3D lattices composed of double-cone elements with small (ideally zero) diameter d at the points where the cone tips merge into small spheres connecting the cones. As an application, we show that tetramode metamaterials can be used as broadband polarizers for transverse metamaterial phonons.

2. Metamaterial Design and Phonon Bands

Figure 1 illustrates the architecture of the tetramode metamaterial considered in this work. It is composed of only a single Cauchy-elastic constituent material and voids within. This constituent is shaped into double-cone elements that are arranged into a metamaterial unit cell that is placed onto a simple-cubic translation lattice with lattice constant a . A tetragonal symmetry metamaterial crystal results. The crucial geometrical parameter of this tetramode metamaterial architecture is the size

or diameter, d , of the regions where the tips of different cones merge into the small spheres with diameter $2r$ connecting the cones (see inset in Figure 1). In our previous work on pentamode metamaterials,^[7–9] we did not use such small spheres but rather connected the cone tips directly. Here, we use the union of spheres and several cone tips to obtain a geometrically well-defined object. Furthermore, the spheres make the structure more tolerant against fabrication imperfections, for example, if the cone tips do not meet perfectly in one point. In the case of $2r > d$ or even $2r \gg d$, the shear stiffness of the connection is still mainly determined by d and only weakly depends on $2r$. The larger diameter at the thick ends of the cones is $D > d$. Clearly, the period a merely scales the frequency and the wave-number, such that the dimensionless parameters determining the qualitative behavior of the tetramode metamaterial are the three ratios d/a , $2r/a$, and D/a .

An ideal effective tetramode material results if one considers the limit $d/a \rightarrow 0$ for the structure in Figure 1. This statement is illustrated by the numerical band-structure calculations (see Experimental Section) depicted in Figure 2. In the three columns of Figure 2, we show three different band structures, for three different ratios of d/a , versus the wavenumber k_z with $\vec{k} = (0, 0, k_z)$. This phonon propagation direction refers to the below experiments. Phonon band structure along the usual tour of the wave vector $\vec{k} = (k_x, k_y, k_z)$ through the high-symmetry points (see inset) of the Brillouin zone of the simple-cubic lattice (which is not the Wigner-Seitz cell of the tetramode metamaterial crystal, cf. Figure 1) are shown in Figure S1 (Supporting Information). In Figure 2, the relevant bands are colored and labeled as x , y , and z , corresponding to the dominant polarization direction of the displacement-vector field. Since for every mode, the displacement polarization is not pure, the designation as x -like, y -like, or z -like is arguably more appropriate but is omitted for the sake of brevity. From the panels of Figure 2, it becomes clear that the maximum frequency of the two lowest bands is shifted to significantly smaller values as the ratio d/a decreases, compared to the maximum frequency of the third lowest band. As a result, the relative frequency range in which only the x -polarized transverse phonon mode can propagate becomes larger as the ratio d/a decreases. To allow for direct comparison with the static elastic properties, we retrieve the effective elasticity matrix of the three cases in Figure 2 by fitting the dispersion relations in the long-wavelength limit (see Supporting Information). Their corresponding six eigenvalues are also shown in the middle row of Figure 2. As expected from the definition of the tetramode metamaterials, four out of the six eigenvalues are at least one order of magnitude smaller than the other two.

To further explain the results in Figure 2, Figure S2a (Supporting Information) illustrates how the metamaterial unit cell can support finite shear stress along the x -direction. In contrast, Figure S2b (Supporting Information) shows that the architecture cannot support shear stress along the y -direction. Likewise, it cannot support normal stress along the z -direction. As a result, elastic waves with y - and z -polarization of the displacement-vector become evanescent for frequencies larger than the maximum frequency of the corresponding bands in Figure 2, whereas waves polarized along the x -direction are still propagating and are transmitted. This combination leads

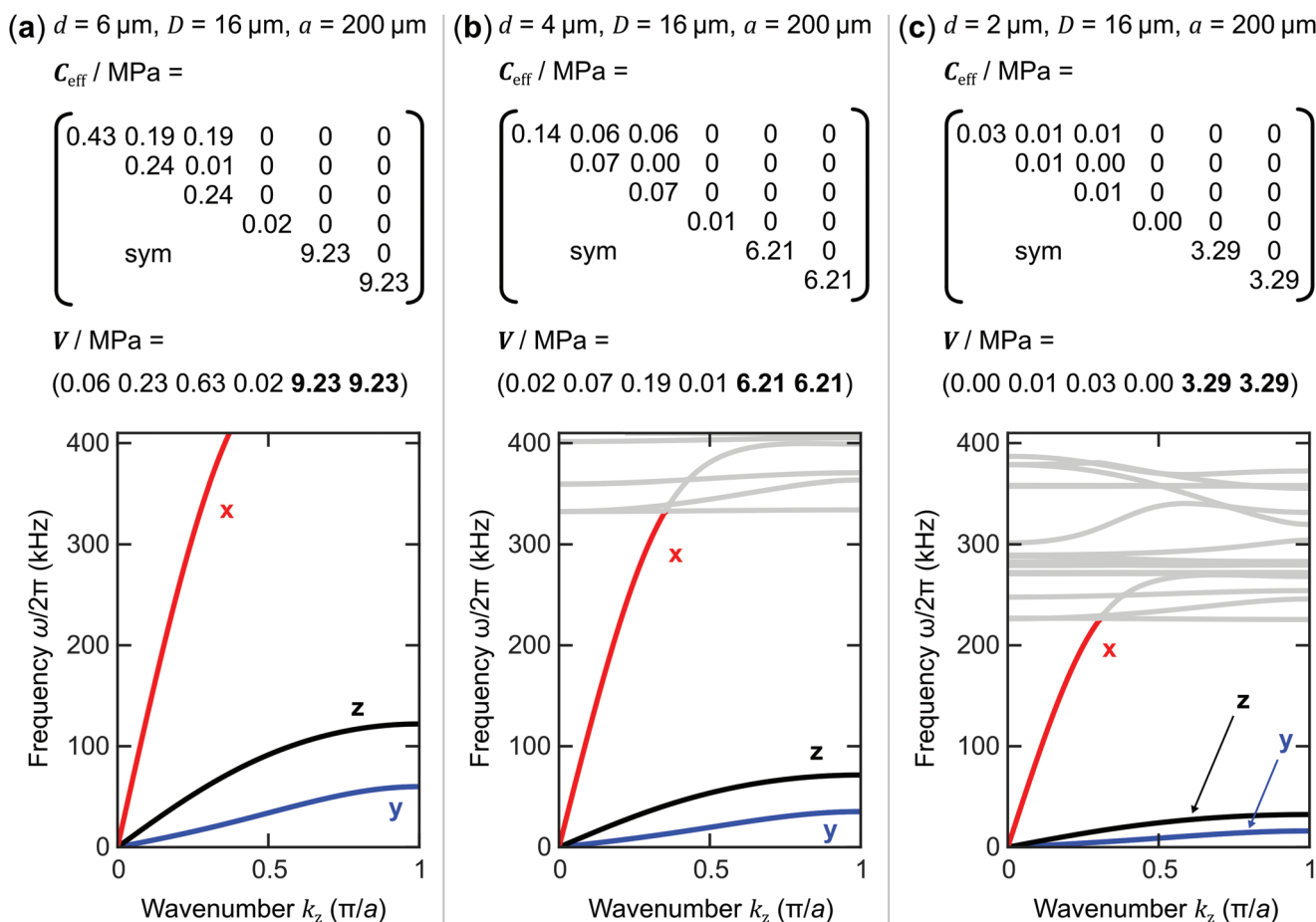


Figure 2. Calculated effective elasticity matrix C_{eff} (in Voigt notation), the respective set of eigenvalues V , and the band structure when varying the critical parameter d , the connection diameter between double-cones and spheres (a–c). The numeric values are rounded to the second digit. Calculations are performed for an infinite sample and are detailed in the Supporting Information. For all parameter choices of d , two out of six eigenvalues are at least one order of magnitude larger than the other eigenvalues. Furthermore, in the band structures, it can be seen how the variation of d influences the maximum frequency of the red and the black or blue bands. Smaller values of d increase the ratio between the maximum frequency of the red band and the respective maximum frequency of the black or blue band. This can also be inferred from the slope of the bands. Reducing d reduces the slope of the two lowest, that is, black and blue bands, while the slope of the third lowest red band remains almost constant. In these plots, the red and the blue band correspond to transverse waves polarized along the x - or y -axis, and the black band to the longitudinal wave polarized along the z -axis. The parameters in panel b) are chosen for the fabrication of the finite-size metamaterial samples.

to a polarizer action that extracts from an arbitrary incident elastic wave with a wave vector $\vec{k} = (0, 0, k_z)$ (cf. Figure 1) and displacement-vector $\vec{u}_{\text{in}} = (u_x, u_y, u_z)$ the transverse component with x -polarization, that is, $\vec{u}_{\text{out}} = (u_x, 0, 0)$ for all inputs. The measurements to be presented below directly record \vec{u}_{in} and \vec{u}_{out} in real space and real time.

3. Comparison Between Experiment and Numerical Results

We have manufactured the samples for these experiments by 3D laser printing (see Experimental Section) using a commercial instrument (Nanoscribe, Photonics Professional GT) and a commercial photoresist (Nanoscribe, IP-S). Each sample is composed of $9 \times 6 \times 6$ unit cells. This particular choice is the result of a trade-off between reasonable printing time (12 h for the $9 \times 6 \times 6$ samples) and good polarizer performance. A gallery

of optical and electron micrographs with different magnifications and different viewing angles onto the polymer tetramode metamaterials is depicted in Figure 3. The targeted geometrical parameters (cf. Figure 1) are: $d = 4 \mu\text{m}$, $D = 16 \mu\text{m}$, and $a = 200 \mu\text{m}$, hence $d/a = 0.02$. Yet smaller ratios of d/a would be desirable, but are not accessible due to the limited spatial resolution of the 3D laser printer. Figure 3 also includes a 3D rendered representation of experimental data acquired by confocal laser-scanning optical fluorescence microscopy (Zeiss, LSM980), showing a single tetramode metamaterial unit cell. Overall, the panels of Figure 3 evidence very high sample quality despite the considerable complexity of the tetramode architecture. However, certain imperfections are visible in Figure 3d. This especially concerns the critical regions in which the cones merge with the spheres (see discussion above). While the cone cross section should be circular where cones and spheres meet, it is actually somewhat elliptical due to the imperfectly compensated ellipticity of the laser focus point-spread function

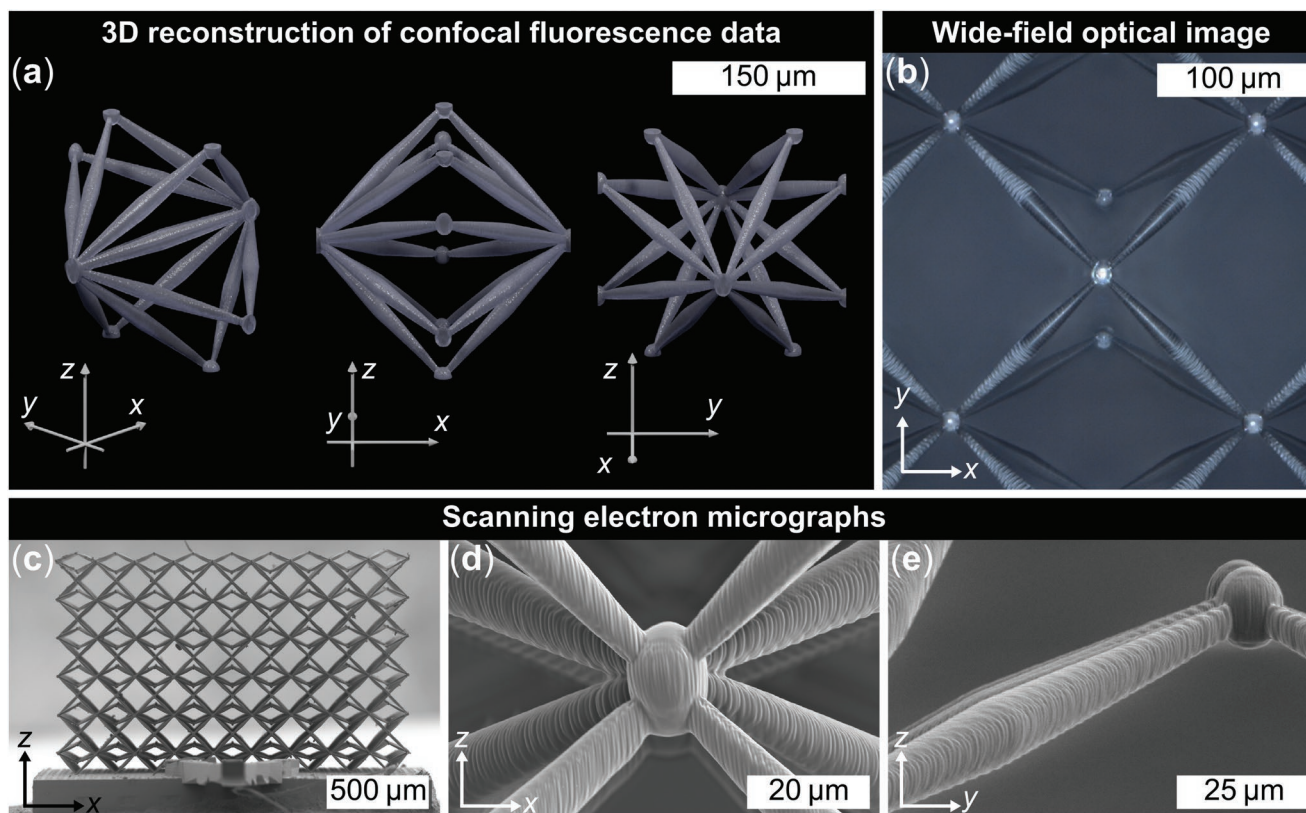


Figure 3. Showcase of different sample features. a) 3D iso-intensity surface of a single unit cell acquired with a laser-scanning confocal fluorescence optical microscope (LSM980, Zeiss) using the autofluorescence of the polymer. Coloring and post-processing were performed in ImageJ and Blender. b) Close-up wide-field image of a sample using the extended depth-of-field feature of a wide-field optical microscope (Smarzoom 5, Zeiss), when imaging along the inverse z-axis. A specular reflection from the LED illumination can be seen in the center as a bright spot. This specular reflection is beneficial for the laser-Doppler vibrometry analysis. c–e) Scanning electron micrographs. c) Side-view of the sample on its bottom plate. The sample shows 9 unit cells along the x- and 6 unit cells along the y- and z-direction. Due to the viewing angle, the cells in the y-direction are not visible. e) Connection of two neighboring unit cells. The anisotropic 3D printing voxel elongates the desired sphere to an ellipsoid. d) Close-up of the region showing the two critical sample parameters, namely the diameter D in the double-cone center and d on the spheres connecting to the cones.

in the 3D laser printer. We have been unable to eliminate these sample imperfections. In fact, it was hard to arrive at the level of quality apparent in Figure 3. Therefore, we rather account for the remaining sample imperfections in the theoretical modeling when comparing experimental and theoretical results below (also see Figure S3, Supporting Information).

The experiments presented in Figure 4 and Figure 5 are conceptually simple, yet technologically demanding. The tetramode metamaterial samples are glued onto piezoelectric-actuator assemblies, which are showcased in Figure 4b,e. By applying a time-harmonic voltage to the respective actuator at variable angular frequency ω , with $\omega/(2\pi)$ from 0 up to 300 kHz, it reacts with a time-harmonic displacement-vector field at the interface between the actuator and metamaterial sample. This constitutes the input displacement $\vec{\mathbf{u}}_{\text{in}} = (u_x, u_y, u_z)$. Generally, depending on the frequency, all three components are nonzero. We measure the local input displacement $\vec{\mathbf{u}}_{\text{in}} = (u_x, u_y, u_z)$ as well as the local output displacement $\vec{\mathbf{u}}_{\text{out}} = (u_x, u_y \approx 0, u_z \approx 0)$ in real time by a dedicated optical setup (see Methods and Supporting Information). This setup allows for measuring the components u_x and u_y by optical confocal image acquisition and subsequent digital image cross-correlation analysis.^[22] The measurement of the u_z component is conducted by laser

Doppler vibrometry.^[23] The latter has not previously been used by us.

In the experiments, two actuator orientations for the excitation of elastic waves are chosen. In the first orientation, the main actuator axis is aligned with the sample z-axis, and in the second orientation along the sample y-axis. The intention behind these orientations is to better showcase the sample performance as a larger input displacement can naturally result in a larger measurable suppression of the unwanted displacement polarization.

Examples of the frequency of $\omega/(2\pi) = 180$ kHz are shown in Figure 4. Here, the measured displacement trajectories, taken at the locations highlighted in red and blue respectively, are shown next to several oblique-view micrographs of the tetramode metamaterial sample.

The input displacement trajectories (red boxes) contain significant components along all three spatial directions, whereas the output displacement trajectory (blue boxes) on the sample top center exhibit $u_y(t)$ and $u_z(t)$ components versus time t , the amplitudes of which are very small compared to that of $u_x(t)$. This behavior corresponds to the anticipated polarizer action. We have also recorded the output displacement trajectories at other positions closer to the sample's edges

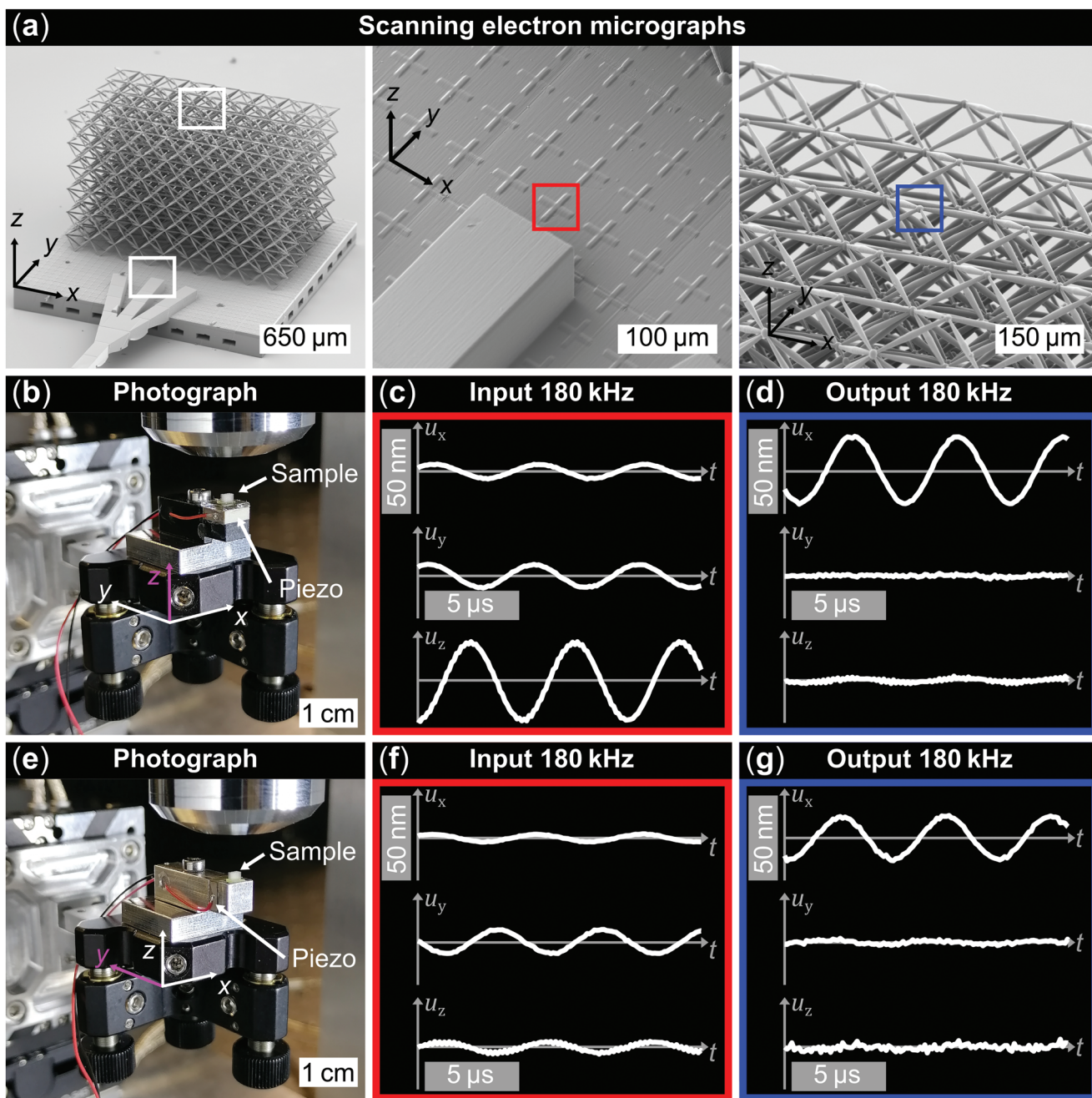


Figure 4. Measurement assemblies and exemplary data sets exhibiting the polarizer functionality. a) Scanning electron micrographs of a sample. The middle and right panels are magnified views of the left panel (see white rectangles). The squares in the middle and right panels highlight the positions which we consider as the “input” (red square) and the “output” (blue square) for our measurements. This color code for input and output is also used in the panels below. b) Photograph of the sample assembly in the measurement setup. The microscope’s objective lens can be seen at the top. A mirror mount is used as a tilt-correction platform for the sample under the objective lens. The sample is glued onto a silica glass substrate which in turn is glued to a piezoelectric actuator (from which cables emerge). The actuator is glued to a PVC mount with the main actuator axis aligned along the z-axis (highlighted in purple). c) Time-resolved evolution of the displacement-vector components as an input to the sample. The x- and y-components of the displacement vector were obtained by optical-image digital cross-correlation analysis. The z-component was obtained using laser Doppler vibrometry. Due to the orientation of the actuator, the input displacement along the z-axis is the largest. d) Corresponding time-resolved displacement output at the sample top. From the displacement raw data, it can be clearly seen how displacements along the y- and z-axis are suppressed and only a significant displacement along the x-axis is left at the sample top. The temporal phase delay between input and output originates from damping within the polymer. The output displacement can exceed the input displacement due to the back reflection of the waves at the top of the sample. e–g) Similar to b–d) but for an assembly where the actuator is glued onto an aluminum mount and where the main actuator axis is aligned with the y-axis (highlighted in purple). To achieve this orientation, the sample is glued onto an aluminum cuboid which serves as an elbow piece. Further photographs of both sample assemblies are shown in Figure S4 (Supporting Information).

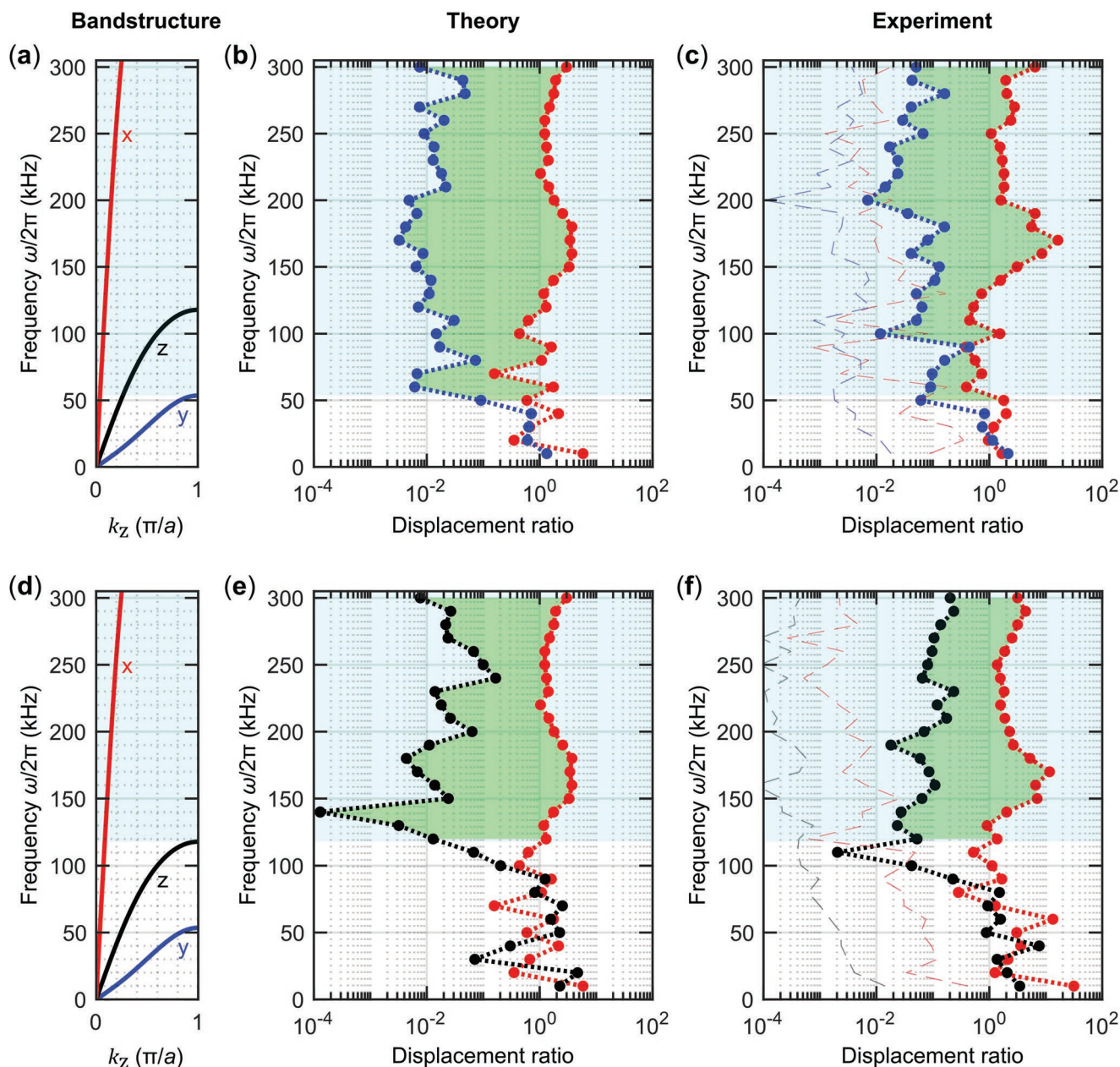


Figure 5. Results as in Figure 4, but shown versus excitation frequency. a,d) Band structure for waves propagating along the sample z-axis with wave number k_z in an infinite bulk. The red and the blue band correspond to transverse waves polarized along the x- or y-axis and the black band to the longitudinal wave polarized along the z-axis. The frequency region of the gap between the a) x- and y-polarized or c) x- and z-polarized modes are highlighted in light blue, respectively. b,e) Displacement ratios computed from theory for the ratio of the excitation displacement-vector components on the sample bottom plate to the vector components of the central point on the sample top. To emphasize the predicted polarizer behavior of the sample, the area between the curves is shaded in light green. c,f) Experimental results for the corresponding displacement ratios. Data from panel (c) was obtained by aligning the piezoelectric actuator main axis along the sample y-axis and in (f) along the sample z-axis. The x- and y-components of the displacement vector were obtained by optical-image digital cross-correlation analysis. The z-component was obtained using laser Doppler vibrometry. A suppression of up to two orders of magnitude is achieved experimentally, when comparing the displacement ratio of the transmitted x-displacement to the ratio of the suppressed y- and z-displacements. In terms of mechanical power, this corresponds to a suppression of up to four orders of magnitude making it well comparable to a polarizer device in optics. The dashed lines indicate the sensitivity limit of the experimental setup. These lines are obtained by calculating the ratio of the excitation displacement-vector components during measurement to a zero-measurement at the sample top where the piezoelectric actuator is not driven.

(not depicted). We find that the polarizer behavior deteriorates due to edge effects, which correspond to a large number of back-folded bands in the band structure of the tetramode

metamaterial beam with finite cross-section shown in Figure 3c and Figure 4a. These back-folded bands are shown in Figure S5 (Supporting Information). Therefore, in what follows,

we concentrate on measuring the output displacement trajectory in the middle of the top of the sample. If larger usable areas should be required in an application, the tetramode metamaterial sample footprint would need to be increased.

Figure 5 summarizes the results of experiments as the example shown in Figure 4, but for many different excitation frequencies from 10 to 300 kHz in steps of 10 kHz. For reference, we depict in the left column band structures for a bulk tetramode metamaterial which is infinitely periodic along all three spatial directions (also cf. Figure 2). The right-hand side column refers to our experiments, which are compared to numerical calculations shown in the middle column of Figure 5 (corresponding data with finer frequency steps of 5 kHz are shown in Figure S6, Supporting Information). For the experiment, the displacement ratios versus frequency show a suppression of the unwanted u_y component of about two orders of magnitude (highlighted by the light green area) for frequencies above 50 kHz. The unwanted u_z component is suppressed by more than one order of magnitude (see light green area) for frequencies above 120 kHz. Both behaviors are in good agreement with theory, but theory tends to predict even slightly better suppressions. We assign this difference to the remaining sample imperfections.

It is interesting to compare the measured broadband-polarizer performance with that of other types of polarizers. The only other published setting that we are aware of and that theoretically allows for separating elastic waves with different polarizations is Reference.^[24] There, different refraction angles at an interface for the different polarizations could be used in the sense of a phonon polarizer. However, experiments are elusive. For optical polarizers, suppression usually refers to the ratio of transmitted intensities, which are proportional to the square of the electric field.^[25] By analogy, we should square the above-mentioned displacement ratios, leading to a suppression of the transverse polarization of about four orders of magnitude. This value is better than that of most wire-grid polarizers used in Fourier-transform spectrometers (see discussion in the introduction). A comparison in regard to the suppression of longitudinal polarization is not possible because electromagnetic waves are usually transversely polarized.

4. Conclusion

Extremal Cauchy-elastic metamaterials exhibit a certain number of easy modes. Ideally, these are connected to zero force or energy needed for the corresponding deformation. Previous work realized pentamode and monomode elastic metamaterials. Here, we have introduced and realized tetramode elastic metamaterials. We have emphasized dynamic wave properties (rather than static properties) because these allow for using tetramode metamaterials as compact and broadband transverse linear elastic polarizers – the so-far missing counterpart to linear polarizers in optics. Our proof-of-principle findings can be improved systematically by further reducing the d/a ratio (cf. Figure 1 and 2) and/or by introducing more metamaterial unit cells along both, the phonon propagation direction, which would enhance the polarizer suppression, and perpendicular

to it, which would reduce the influence of edge effects, hence increase the usable polarizer area.

5. Experimental Section

Numerical Band Structure Calculations: Phonon band structures (c.f. Figure 2) for the tetramode metamaterials were numerically obtained by using the Solid Mechanics Module of the commercial software package COMSOL Multiphysics. Bloch-periodic boundary conditions were applied to the six surfaces of the cubic unit cell (cf. Figure 1). All other boundaries were stress-free. The solved mathematical equations for the linear elastic-wave propagation problem are provided in the Supporting Information (cf. Equation (S1), Supporting Information). For the band structures depicted in Figure 2, the Bloch wave vector was only swept, $\mathbf{k} = (0, 0, k_z)$ from $(0, 0, 0)$ to $(0, 0, \pi/a)$. More complete results for tetramode metamaterials are shown in Figure S1 (Supporting Information). There, the usual tour of wave vectors along high-symmetry directions through the first Brillouin zone of the simple-cubic lattice was considered.

Tetramode Sample Fabrication: The tetramode metamaterial samples were fabricated by 3D laser microprinting (Professional GT, Nanoscribe). A $25 \times$ objective lens with a numerical aperture of 0.8 (Carl Zeiss) was dipped into the liquid photoresist (IP-S, Nanoscribe). The laser focus was scanned by two galvanometric mirrors at a focus velocity of 0.110 m s^{-1} . The mean laser power at the entrance pupil of the objective lens was set to 37.5 mW. The 3D model of the sample was created with a commercial software package COMSOL Multiphysics (COMSOL Inc.). The model was processed with the commercial software Describe (Nanoscribe) to generate machine code for the 3D laser printer. A hatching distance of 300 nm and a slicing distance of 500 nm were chosen. For printing, the model of the unit cell was split up into parts that were printed sequentially. This guaranteed well-defined connections between the individual parts and alleviated the fabrication of overhanging sections of the unit cell. Each sample was printed onto a bottom plate with a small handle. This facilitated the manipulation of the samples and ensured proper contact of the samples when glued on a piezoelectric-actuator assembly. The bottom plates were written with a focus velocity of 0.140 m s^{-1} , a hatching distance of 500 nm, and a slicing distance of $1.5 \mu\text{m}$. After printing, the samples were rinsed in a beaker of propylene glycol methyl ether acetate for at least 30 min to remove the excess photoresist. To prepare for critical point drying with CO_2 (Leica, EM CPD300), the samples were rinsed again with acetone for ≈ 5 min. Further detail on the printing parameters and the printing sequence could be extracted from the GWL files included in the data repository and published with this work (<https://dx.doi.org/10.35097/935>).

Experiment Setup: The tetramode sample was glued onto a piezoelectric-actuator assembly. The gluing process is illustrated in more detail in Figure S7 (Supporting Information). The main axis of the piezoelectric actuator (Physik Instrumente, PL055.31 PICMA) was either aligned with the sample y - or z -axis. The sample exceeded the field of view of the optical measurement setup. Therefore, the assembly was mounted on an xyz -translation stage with piezo-inertia drives (Physik Instrumente, Q-545) for manipulation of the sample. For the measurement, the region of interest on the sample was positioned in the focal plane of the microscope objective lens (cf. Figure S8, Supporting Information) which resulted in a top-view of the tetramode sample, along the inverse z -axis. The back-reflected light was measured by two avalanche photodiode modules. The first module (APD1) belonged to the optical confocal imaging mode. It outputted a photovoltage proportional to the incident light power. The second module (APD2) served the heterodyne laser Doppler vibrometry mode. The output Doppler signal voltage was proportional to the AC component of the interfering electric fields of the back-reflected light and a frequency-shifted reference beam. The frequency shift was generated by an acousto-optic modulator (AA, MT80-A1.5-VIS).

Single-Frequency Excitation Measurement: The mechanical excitation of the tetramode samples was achieved by driving the piezoelectric

actuator with an amplified sinusoidal voltage. The data acquisition units of the optical setup were synchronized to this drive signal to ensure the retrieval of the correct temporal phase information of the measured displacement-vector components.

The data acquisition was split into two channels, corresponding to the optical imaging mode and the laser Doppler vibrometry mode, respectively. For the optical imaging, spatial regions of interest (ROIs) on the excited sample were scanned. Each ROI was divided into 60×60 pixels and spanned a region of $30 \times 30 \mu\text{m}$. At every pixel, a time series of the photovoltage from APD1 was recorded, sequentially. Afterward, for the laser Doppler vibrometry mode, a time series of the APD2 output voltage was recorded at the central pixel of the current ROI before moving on to the next. In total, four ROIs were measured on every sample. Three ROIs were spaced $\approx 750 \mu\text{m}$ apart, including cross-shaped markers on the sample bottom plate. After averaging, the data represented the displacement input to the sample. The fourth ROI was located at the sample top center and was considered the displacement output.

The excitation frequency was incremented in steps of $\Delta f = 10$ kHz from 0 to 300 kHz and was held constant until all ROIs on the sample were measured for that frequency. A buffer of ≈ 200 ms in the data acquisition was included between switching of the excitation frequency. This ensured that the sample had sufficient time to respond to the new excitation.

To form images for the digital image cross-correlation analysis, the time series were combined while considering the synchronization between data acquisition and the drive signal^[22] (cf. Figure S9, Supporting Information). The demodulation and digital signal processing for the laser Doppler vibrometry were implemented as a digital IQ-demodulator using the arctangent phase method (cf. Figure S10, Supporting Information).^[26]

Supporting Information

Supporting Information is available from the Wiley Online Library or from the author.

Acknowledgements

M.F.G., J.L.G.S., and Y.W. contributed equally to this work. The authors thank the Deutsche Forschungsgemeinschaft (DFG, German Research Foundation) under Germany's Excellence Strategy via the Excellence Cluster "3D Matter Made to Order", EXC-2082/1-390761711 (MW), the Carl Zeiss Foundation through the "Carl-Zeiss-Foundation-Focus@HEiKA" (MW), the State of Baden-Württemberg (MW), the Helmholtz program "Materials Systems Engineering" (MW), the Alexander von Humboldt Foundation (YC), the EIPHI Graduate School ANR-17-EURE-0002 (MK), and the National Natural Science Foundation of China (Grants No. 11632003, No. 11972083, No. 11991030) (GH) for financial support. The authors thank F. Decker for advice on the design of the digital signal processing and P. Scott for assistance with the scanning electron micrographs.

Open access funding enabled and organized by Projekt DEAL.

Conflict of Interest

The authors declare no conflict of interest.

Data Availability Statement

The data that support the findings of this study are openly available in KIT Repository at [https://dx.doi.org/10.35097/935].

Keywords

elastic waves, metamaterials, phonons, polarizations, tetramode materials, ultrasound experiments

Received: December 16, 2022

Revised: January 24, 2023

Published online:

- [1] A. E. H. Love, *A Treatise on the Mathematical Theory of Elasticity*, 4th ed., Cambridge University Press, Cambridge, UK **1952**.
- [2] G. W. Milton, *The Theory of Composites*, Cambridge University Press, Cambridge, UK **2002**.
- [3] G. W. Milton, A. V. Cherkaev, *J. Eng. Mater. Technol.* **1995**, *117*, 483.
- [4] C. N. Layman, C. J. Naify, T. P. Martin, D. C. Calvo, G. J. Orris, *Phys. Rev. Lett.* **2013**, *111*, 24302.
- [5] Z. Li, Z. Luo, L. Zhang, C. Wang, *Mater. Des.* **2021**, *202*, 109523.
- [6] G. W. Milton, *J. Mech. Phys. Solids* **2013**, *61*, 1543.
- [7] M. Kadic, T. Bückmann, N. Stenger, M. Thiel, M. Wegener, *Appl. Phys. Lett.* **2012**, *100*, 191901.
- [8] M. Kadic, T. Bückmann, R. Schittny, M. Wegener, *New J. Phys.* **2013**, *15*, 023029.
- [9] A. Martin, M. Kadic, R. Schittny, T. Bückmann, M. Wegener, *Phys. Rev. B* **2012**, *86*, 155116.
- [10] M. Kadic, T. Bückmann, R. Schittny, P. Gumbsch, M. Wegener, *Phys. Rev. Appl.* **2014**, *2*, 54007.
- [11] A. N. Norris, *Proc. R. Soc. A* **2008**, *464*, 2411.
- [12] T. Bückmann, M. Thiel, M. Kadic, R. Schittny, M. Wegener, *Nat. Commun.* **2014**, *5*, 4130.
- [13] Y. Chen, M. Zheng, X. Liu, Y. Bi, Z. Sun, P. Xiang, J. Yang, G. Hu, *Phys. Rev. B* **2017**, *95*, 180104.
- [14] A. N. Norris, *J. Acoust. Soc. Am.* **2009**, *125*, 839.
- [15] K. F. Graff, *Wave Motion in Elastic Solids*, Dover Publications, New York, USA **2012**.
- [16] L. Guo, *Adv. Mater.* **2007**, *19*, 495.
- [17] M. Xu, H. Urbach, D. de Boer, H. Cornelissen, *Opt. Express* **2005**, *13*, 2303.
- [18] S. Ahn, K. Lee, J. Kim, S. H. Kim, J. Park, S. Lee, P. Yoon, *Nanotechnology* **2005**, *16*, 1874.
- [19] L. D. Barron, *Molecular light scattering and optical activity*, Cambridge University Press, Cambridge, UK **2004**.
- [20] Y. Wei, X. Liu, G. Hu, *Mater. Des.* **2021**, *210*, 110031.
- [21] Y. Wei, G. Hu, *Extreme Mech. Lett.* **2022**, *55*, 101789.
- [22] J. A. I. Martínez, M. F. Groß, Y. Chen, T. Frenzel, V. Laude, M. Kadic, M. Wegener, *Sci. Adv.* **2021**, *7*, m2189.
- [23] C. Rembe, A. Dräbenstedt, *Rev. Sci. Instrum.* **2006**, *77*, 083702.
- [24] H. Liu, Q. Zhang, K. Zhang, G. Hu, H. Duan, *Adv. Sci.* **2019**, *6*, 1900401.
- [25] S. Y. Kim, J. Gwyther, I. Manners, P. M. Chaikin, R. A. Register, *Adv. Mater.* **2014**, *26*, 791.
- [26] C. Rembe, G. Siegmund, H. Steger, M. Wörtge, in *Optical Inspection of Microsystems*, 2nd ed., CRC Press, Boca Raton, FL, USA **2019**, p. 584.